Journal of Materials Science & Technology 134 (2023) 244–253

Contents lists available at ScienceDirect

Journal of Materials Science & Technology

journal homepage: www.elsevier.com/locate/jmst

Research Article

The martensitic transition pathway in steel

Tianwei Liu[a,b], Lunwei Liang[a,b], Dierk Raabe[c,*], Lanhong Dai[a,b,*]

[a] State Key Laboratory of Nonlinear Mechanics, Institute of Mechanics, Chinese Academy of Sciences, Beijing 100190, China
[b] School of Engineering Science, University of Chinese Academy of Sciences, Beijing 101408, China
[c] Max-Planck-Institut für Eisenforschung, Düsseldorf, Germany

ARTICLE INFO

Article history:
Received 24 March 2022
Revised 18 May 2022
Accepted 16 June 2022
Available online 18 July 2022

Keywords:
BCT twin
Martensitic transformation
Steels
TEM
Phase transformation

ABSTRACT

The martensitic transformation (MT) lays the foundation for microstructure and performance tailoring of many engineering materials, especially steels, which are with > 1.8 billion tons produced per year the most important material class. The atomic-scale migration path is a long-term challenge for MT during quenching in high-carbon (nitrogen) steels. Here, we provide direct evidence of $(1\bar{1}2)$ body-centred tetragonal (BCT) twinned martensite in carbon steels by transmission electron microscopy (TEM) investigation, and the increase in tetragonality with the C content matches X-ray diffraction (XRD) results. The specific $\{1\bar{1}2\}_{BCT}$ twin planes which are related to the elongated *c* axis provide essential structural details to revisit the migration path of the atoms in MT. Therefore, the face-centred cubic (FCC) to BCT twin to body-centred cubic (BCC) twin transition pathway and its underlying mechanisms are revealed through direct experimental observation and atomistic simulations. Our findings shed new light on the nature of the martensitic transition, thus providing new opportunities for the nanostructural control of metals and alloys.

1. Introduction

Martensite is both an important transformation mechanism and an essential microstructure ingredient. It forms one of the main pillars of hardening steels and several other alloy classes and is thus widely used in materials science since it was first identified in steels in the late 19th century [1–7]. The martensitic transformation (MT) belongs to the category of displacive crystalline structural phase transformations [8–11]. The most basic and important MT is the formation of a metastable body-centred tetragonal (BCT) phase in steels. Although the first scientific investigations on the MT date back only about 130 years, it was used in steels already about 2800 years ago as an important strengthening mechanism [8–13]. The ambition to understand the atomistic nature of this transformation in its immense importance in engineering has motivated huge efforts to explore the associated mechanisms, including such seminal works as those related to the Bain mechanism [14], the K–S orientation relationship (OR) [15], the Pitsch OR [16], the BBOC model [17,18], and many others [19–27].

Due to the high rate of the MT (close to the speed of sound), it is difficult to observe the transformation process directly. Most current interpretations of the MT mechanism are based on the structure characteristics of the material in its face-centred cubic (FCC) initial state and in the final body-centred cubic (BCC) or BCT state after the transformation [17–27]. The martensite appears as a BCT lattice structure in X-ray diffraction (XRD) experiments, and the double peaks that are characteristic of the BCT structure are increasingly separated from each other with increasing carbon (or nitrogen) content [28,29]. However, when aiming at obtaining more detailed structural insights on martensite by transmission electron microscopy (TEM), the results were often disappointing, in contrast to XRD experiments [30–34]. The reason is that BCT martensite can lose some of its typical structure characteristics (such as the degree of tetragonality) in TEM observations as some of the frozen-in interstitials can relax upon specimen preparation. However, other features such as twins remain visible after exposing the steels to TEM preparation. Twins occur as a very important substructure feature of martensite in steels with 0.1 wt.% to 1.6 wt.% C, and these have long been identified as {112}<111>-type BCC twins, as in other BCC metals and alloys [30–34]. The contradiction between TEM and XRD results, therefore, has made it often more difficult to comprehend the MT process. Additionally, due to the different possible arrangements of the interstitials in the martensitic lattice and the effect of Zener ordering [20,35], the exact positioning and migration paths of the atoms involved during the phase transformation process are unclear. Also, even if recent theoretical progress provides a clearer picture of the ordering preferences of interstitial

* Corresponding authors.
E-mail addresses: d.raabe@mpie.de (D. Raabe), lhdai@lnm.imech.ac.cn (L. Dai).

https://doi.org/10.1016/j.jmst.2022.06.023
1005-0302/

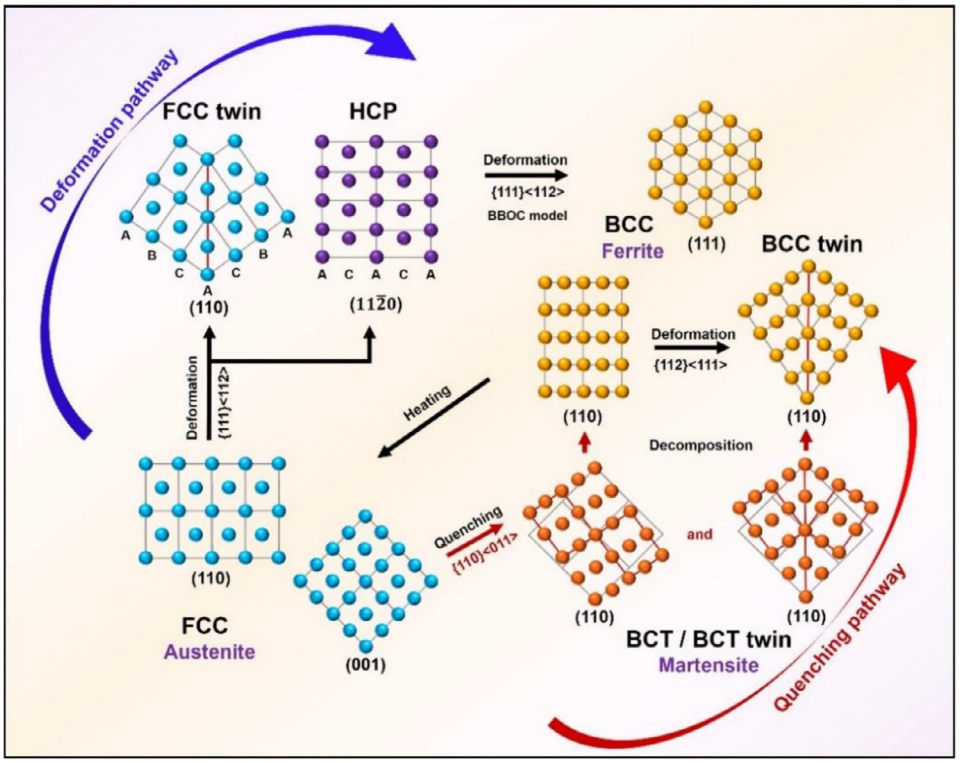

Fig. 1. Overview figure for the twinning and transformation processes in steels and related alloys. There are two possible pathways for the phase transition from FCC to BCC: the deformation pathway, with a transition from FCC to HCP and then to BCC (the BBOC model) [17,18] and the quenching pathway, with a transition from FCC to a BCT/BCT twin and then to a BCC/BCC twin.

C atoms in martensite [36–39], the processes during the transition remain unclear.

To resolve these basic issues associated with the MT, we analyse the individual transformation steps here one by one, using theoretical and experimental methods. We use electron diffraction through reciprocal space probing and atomistic modelling as tools for a pseudo-*in-situ* investigation on the dynamics of the martensitic transformation process. The methodology refers to the reconstruction of the individual process steps by obtaining the relevant information in different states from a series of stepwise experiments and their atomistic analysis. We start by revisiting the core contradiction mentioned above and clearly show that BCT twins do indeed exist in high-carbon steels by TEM and electron diffraction analysis. By identifying the unique structural characteristics and evolution of the intermediate state BCT twin, we are further able to validate the entire phase transformation process. More specific, a transformation from BCT twin to BCC twin is directly observed, and based on this finding we propose a new phase transformation mechanism following the sequence FCC to BCT twin to BCC twin which is different from the BBOC model usually observed in deformation-driven transformation processes [17,18,40–42] (Fig. 1). The BBOC model was proposed in 1960–1970 [17,18], and verified and developed in recent years [40–42]. Using the information about the symmetry of the BCT twin and the orientation relationships (OR) among these three structures, we introduce a new transformation model and explain the underlying atomic migration paths during the MT. We do not only discuss the positions of the Fe atoms but also clarify the transition pathway of the interstitial C atoms from their initially disordered to an ordered arrangement in the host lattice during the course of the phase transition process. The proof of the existence of a BCT twin and its formation mechanism shed new light on the MT. This provides knowledge-based access to improved structural control of steels and other alloys, such as high entropy alloys that contain interstitial atoms in solid solution. It can also serve to tune specific functional properties, such as magnetic anisotropy, in addition to the mechanical properties of alloys [43–48].

2. Experimental procedure

Fe-C ingots with different C contents (0.8 wt.% (3.58 at.%), 1.0 wt.% (4.45 at.%), and 1.4 wt.% (6.14 at.%)) were prepared in a high vacuum induction furnace under argon atmosphere and hot forged. Plates (50 mm × 20 mm × 2 mm) were mechanically sectioned and austenitized at 1473 K for 1 h under an argon atmosphere, followed by ice-water quenching. Quenched samples were detected by an XRD diffractometer (Rigaku SMARTLAB) equipped with Cu-*Ka* radiation, operated at 45 kV and 200 mA. The specimens for TEM observation were prepared by mechanical grinding and polishing to a thickness of approximately 50–70 μm and then subjected to twin-jet electropolishing. The electrolyte consisted of 5%-$HClO_4$, 75%-H_2O, and 20%-$C_3H_5(OH)_3$. The microstructural observation was carried out with a JEM 2100F instrument operated at 200 kV. The heating rate during the *in-situ* TEM observations was approximately 15 K/min. Electron diffraction and XRD analyses were performed using CrystalMaker (CrystalMaker Software Ltd) and JADE (MDI) softwares.

The needle-shaped specimens required for atom probe tomography (APT) were fabricated by lift-out and annular milling in an FEI Scios focused ion beam/scanning electron microscope (FIB/SEM). APT characterization was then performed in a local electrode atom probe instrument (CAMECA LEAP 5000 XR). The specimens were analysed at 50 K in voltage mode at a pulse repetition rate of 200 kHz, a pulse fraction of 20%, and an evaporation detection rate of 0.5% atoms per pulse. Imago Visualization and Analysis

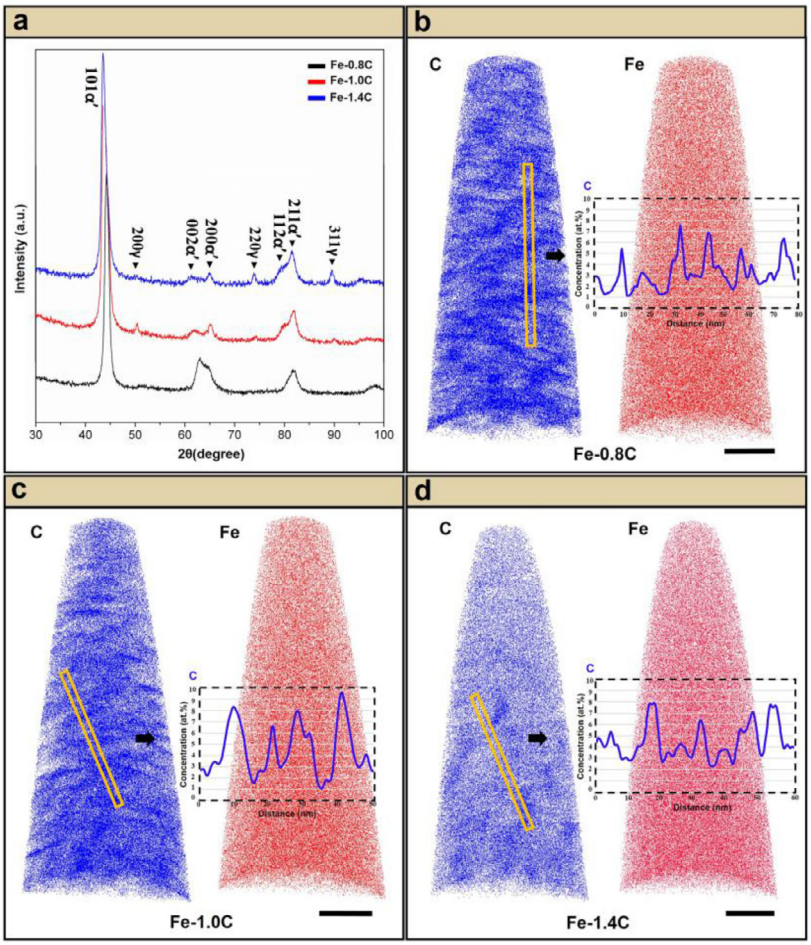

Fig. 2. XRD (a) and APT results (b–d) of as-quenched Fe-C specimens with different nominal bulk C contents (0.8 C, 1.0 C, and 1.4 C (wt.%)). The results show that C atoms are not uniformly distributed inside the martensite, and the average C contents of the entire APT tips are far below these nominal values. The black scale bar in (b–d) is 20 nm.

Software (IVAS) version 3.8 was used to create the 3D reconstructions and for data analysis.

3. Results and discussion

3.1. Observation of the BCT twin

Fe-C Specimens with different C contents (0.8 wt.% (3.58 at.%), 1.0 wt.% (4.45 at.%), and 1.4 wt.% (6.14 at.%)), quenched from 1473 K, were examined by XRD, as shown in Fig. 2(a). In the XRD results, martensite is the main structure, and some retained austenite exists in the 1.0 C and 1.4 C (wt.%) specimens. The double peaks $(002)_{\alpha'}$ and $(200)_{\alpha'}$ of BCT martensite become more distinct and also slightly more separated from each other with increasing C content, consistent with earlier reports [8,9,28,29]. The c/a ratios of martensite in these specimens were calculated from the XRD peaks as 1.031, 1.046, and 1.056 (BCT: $a < c$) by JADE software, respectively. To confirm the C content that contributes to the tetragonality of the martensite, APT experiments were carried out (Fig. 2(b–d)). For the three alloys, the APT results indicate an average C content of approximately 0.6 wt.% (2.73 at.%), 0.89 wt.% (4.01 at.%), and 1.08 wt.% (4.83 at.%), respectively, when integrated over the entire APT tips. The data also reveal that the distributions of the C atoms (from about 1 at.% to 9 at.%), which are shown in the insets of Fig. 2(b–d), are not as uniform as Fe atoms. The APT data show that (i) the real C content inside of the martensite is substantially lower than the alloys' nominal C content, and (ii) the C atoms are not uniformly distributed inside the martensite. Many studies have pointed out that C partitioning from martensite into (retained) austenite can occur during cooling [49]. Also, short-range motion and segregation of C atoms to lower energy positions inside the martensitic microstructure occur during water-quenching, as C can conduct a few atomic jumps prior to being frozen in [47]. Inside the martensite, C atoms tend to segregate to dislocations, lath boundaries, grain boundaries, and other lattice defects [50–52]. Therefore, the true C content inside the martensite is below the nominal one due to C partitioning into austenite and trapping of C atoms at high-angle grain boundaries [49,50]. Also, the C distribution shows substantial variations inside the martensite. C decorates dislocation cores and dislocation boundaries, and the excess of C at these defects increases with increasing dislocation density [51]. The C content on the interstitial positions of the martensite, thus contributing to its tetragonality, therefore remains below the average content, as a substantial fraction of C is located at dislocations or substructure boundaries [50–52], as shown in Fig. 2(b–d). C atoms have also been suggested to cluster on the interstitial sublattice, following a spinodal mechanism [53–55]. In this process, C atoms redistribute and form compositional waves but maintain their adherence to the same interstitial sublattice, and thus the martensitic lattice remains in a state of tetragonal distortion [53]. As shown in Fig. 2(b–d), nanocarbides have not been observed. To proof and evaluate the precision in the analysis of

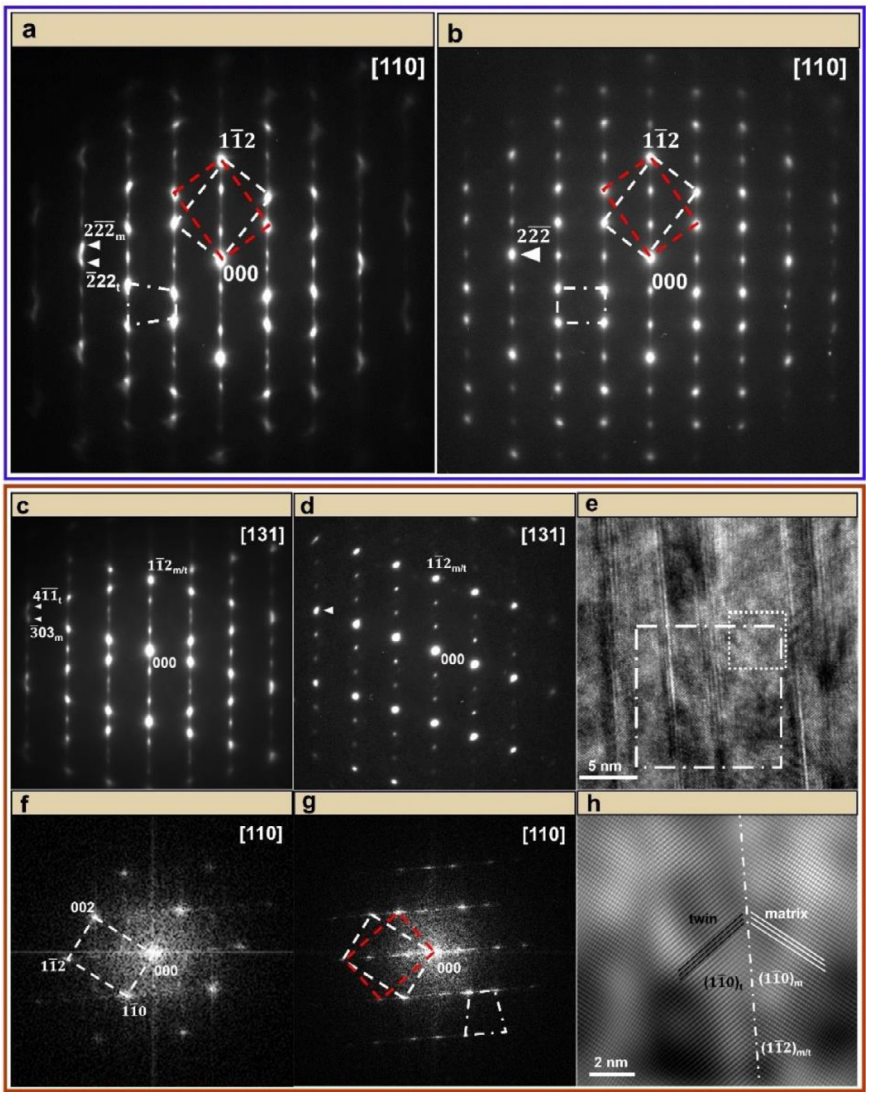

Fig. 3. TEM images of twinned martensite in the Fe-1.4C specimen. (a) SAED pattern of BCT twinned martensite along the [110] ZA. Diffraction spots from the matrix and twin are indicated by the white and red dashed lines, respectively. (b) SAED pattern of BCC twinned martensite along the [110] ZA as reported in previous studies. (c) SAED pattern of BCT twins along the [131] ZA tilted from (a). (d) SAED pattern of BCC twins along the [131] ZA as in previous studies. (e) HRTEM image of BCT twinned martensite. (f) FFT pattern of the region outlined by the dotted frame in (e). (g) FFT pattern of the region outlined by the dotted-dashed frame in (e). (h) Inverse FFT image of (e) displaying the twin lattice. The white row of lines, the black row of lines, and the white dotted-dashed line indicate the $(1\bar{1}0)_m$ planes, $(1\bar{1}0)_t$ planes, and $(1\bar{1}2)_{m/t}$ twin boundary, respectively. (Subscripts m and t indicate matrix and twin.)

the C distribution inside the martensite, the mass-to-charge spectra of all three alloys are shown in Fig. S1 in the Supplementary Materials.

In previous investigations [28–32], the structure of martensite has been widely studied. The selected area electron diffraction (SAED) pattern of twinned martensite observed in the current study (Fig. 3(b)) is consistent with that of {112}<111>-type BCC twins found for other BCC metals and alloys [33,34] and with the corresponding simulation (Fig. S3(b)). However, since the aspect ratio of the BCT structure is different from that of the BCC structure, the SAED spots obtained for the BCT structure deviate from the positions of those that are obtained for the BCC lattice. Therefore, some diffraction spots which overlapped in BCC twins could be separated in BCT twins, and this separation of the diffraction spots would become more distinct and thus detectable with increasing c/a axial ratio.

To shed light on the contradiction between the martensite's BCT structure as observed by XRD [28,29] and that observed in TEM as BCC twin in previous studies [30–34], detailed TEM observations and electron diffraction analyses were carried out on several specimens of the three Fe-C alloys. In order to reduce the influence of the heat treatment and preparation process on the TEM observation, a high homogenization temperature (1473 K) and a fast quenching rate were selected. TEM foils were prepared via double-jet electropolishing on freshly quenched specimens to avoid the influence of ion beam damage on the martensite. Due to the symmetry of the twin, the difference between the BCC and BCT structures can be readily distinguished by electron diffraction analysis, and the c/a ratio can also be revealed in TEM. The specimen with the highest c/a ratio (Fe-1.4wt.%C) was at first selected for probing, and more detailed observations of martensite were carried out along the zone axes (ZA) (<110>, <131>, and <120> families) where twin diffraction spots can be observed.

Fig. 3(a) shows a SAED pattern of twinned martensite along the [110] ZA which is different from that of the BCC twin shown in previous studies (Fig. 3(b)) [30–34]. To further confirm the twin structure, the specimen was tilted approximately 30° from the [110] ZA to the [131] ZA. The corresponding SAED pattern

(Fig. 3(c)) is also different from that of the BCC twin taken along the [131] ZA (Fig. 3(d)) [31,33]. Diffraction spots $(30\bar{3})_m$ and $(\bar{4}11)_t$ are separated in Fig. 3(c), while they overlap in the BCC twin (Fig. 3(d)). To reduce the influence of foil thickness on the SAED signal and further confirm the SAED pattern observed, additional high-resolution TEM (HRTEM) observations were carried out as shown in Fig. 3(e). The Fourier-filtered transformed (FFT) diffraction pattern (Fig. 3(g)) from the matrix and the twin region is the same as that in Fig. 3(a). Fig. 3(f) from the matrix region is used as a reference structure for comparison with Fig. 3(g). According to this observation (Fig. 3), the twin structure can reasonably be considered a BCT twin where one of the {112} planes is the twin plane, confirming the general picture of the MT. (For the morphology of the BCT and BCC twins, see Fig. S2)

To further study the twinned martensite observed in Fig. 3, a detailed electron diffraction analysis of the BCC twin and the BCT twin has been conducted as shown in the Supplementary Materials and in Fig. S3. The diffraction spots (Fig. S2(f)) overlap very well between the simulation pattern of the BCC twin (Fig. S3(b)) and the TEM observation (Fig. 3(b)). The simulated diffraction pattern of the BCT twin shown in Fig. S3(d) also matches the TEM observation (Fig. 3(a)) very well, and the overlapped image is shown in Fig. S2(c). Based on this TEM observation (Fig. 3) and the electron diffraction analysis (Fig. S3), several differences can be identified in the diffraction patterns along the [110] ZA between the BCC and the BCT twin. A trapezoidal shape is formed by the matrix and twin diffraction spots in the BCT twin, and only the gradient direction of the trapezoid shown in Fig. 3(a) could be observed. Moreover, diffraction spots $(2\bar{2}\bar{2})_m$ and $(\bar{2}22)_t$ differ from each other in the BCT twin, while they overlap with each other in the BCC twin, due to the structure's higher symmetry. In addition, extra diffraction spots between $(1\bar{1}2)$ and (000) are located at the 1/3 and 2/3 $(1\bar{1}2)$ positions in the BCC twin, while they deviate from these positions in the BCT twin.

3.2. Characteristics of BCT twins for different c/a ratios

The c/a ratio of the BCT structure increases with the C content, as revealed by the XRD results (Fig. 2(a)), in agreement with the general understanding of the MT and the associated Zener ordering of the C [20]. This macroscopic result motivated us to probe this C dependence also by TEM. The experimentally observed diffraction patterns of BCT twinned martensite with different C contents (1.4 C, 1.0 C, and 0.8 (wt.%) C) are shown in Fig. 4(a–c). With an increasing c/a ratio, the structural features of the BCT twin become more obvious. The higher the c/a ratio is, the larger the gradient of the trapezoidal shape in the diffraction patterns is, and the larger the separation of the $\{2\bar{2}\bar{2}\}$ diffraction spots are. In other words, with decreasing C content, the trapezoidal shape of the BCT twin changes into a rectangular shape as that in the BCC twin. The calculated diffraction patterns (Fig. 4(g–i)) with c/a ratios of 1.056, 1.046, and 1.031, respectively, match those obtained from the TEM observations (Fig. 4(a–c)). Therefore, the TEM observations (Fig. 4(a–c)) are consistent with the XRD results (Fig. 2(a)), when considering the TEM instrument error, minor differences in local C concentration among different martensite regions probed in TEM and the statistics associated with XRD probing.

3.3. Phase transformation from BCT twin to BCC twin

In the common view, BCT Fe-C martensite forms from FCC austenite during quenching and subsequently decomposes into BCC ferrite and carbides during tempering [8,9]. Therefore, an FCC to BCT twin to BCC twin transformation sequence can in principle exist during the course of the MT process, as confirmed by the BCT twin martensite observation in the present study. Fig. 4(a) shows the SAED pattern of the BCT twin at 300 K. The virgin Fe-C martensite is unstable, and phase separation will occur by a spinodal mechanism prior to carbide precipitation [53–55]. The spinodal decomposition is characterized by a redistribution of the C atoms on their octahedral interstitial sites in the martensite, an effect that produces diffuse electron scattering [53–55]. Fig. 4(d) shows clear diffuse scattering around the diffraction spots, which means that spinodal decomposition occurred in specimens after ageing at room temperature (RT) for 3 days. *In-situ* heating experiments conducted in the TEM (Fig. 4(a, e, f)) show that the c/a ratio of the BCT twins decreases with increasing temperature. The gradient of the trapezoidal shape decreases, while the $(2\bar{2}\bar{2})_m$ and $(\bar{2}22)_t$ spots shift closer to each other. Finally, the trapezoid changes to a rectangle, and the $(2\bar{2}\bar{2})_m$ and $(\bar{2}22)_t$ spots overlap with each other at 673 K, as in a BCC twin. Some weak diffraction spots are gradually produced in the SAED patterns (Fig. 4(e, f)), indicating that carbides have formed during tempering. Comparing the insets in Fig. 4(e, f), the thickness of the twin structure is obviously increasing, indicating that the de-twinning process occurs concurrently. In addition, it is found that the c/a ratio is still above 1 in the material's state shown in Fig. 4(e) but smaller than that in Fig. 4(a). The morphology and thickness of the twin structure (insets in Fig. 4(a, e)) exhibit only minor changes. This means that C atoms diffuse from the BCT crystal lattice and begin to form nanoscale carbide particles. With increasing temperature, the c/a ratio of the BCT lattice finally decreases to 1 (at 673 K), and nanoscale carbide particles further develop into cementite. To further confirm the BCT twin to BCC twin process, *in-situ* heating experiments on another reference specimen of the same state (1.4 wt.% C) have been conducted and probed along the [131] ZA, and the same conclusion was reached.

3.4. Martensite transformation stage from FCC to BCT twin

The atomic-scale migration processes from FCC to BCT are difficult to observe directly, due to the near-sonic transformation rate. Yet, the observation of the BCT twin provides sufficient experimental evidence to revisit this step of the MT process, especially the existence of a specific $(1\bar{1}2)_{BCT}$ twin plane related to the elongated c axis. As mentioned in the section about the electron diffraction analysis (Supplementary Materials), the twin plane is the $(1\bar{1}2)_{BCT}$ plane, but this brings the question of what the corresponding matching plane in the hosting FCC structure is. In previous studies, numerous orientation relationships (ORs) between austenite and martensite were studied (Table S2). Several theoretical models have been proposed to interpret both the underlying ORs and the habit planes, such as the phenomenological theory of martensitic crystallography [14–16,21–23] and the O-lattice theory [56]. As in the Bain correspondence [14], the $\{1\bar{1}2\}_{BCT}$ plane corresponds to the $\{110\}_{FCC}$ plane during the MT and has been investigated in numerous studies [16,21]. If the c/a ratio is assumed to be 1.056, the $[\bar{1}10]_{FCC}$ and $[\bar{1}11]_{BCT}$ directions are very similar in length and they also have a similar atomic arrangement as they are the close-packed directions in austenite and martensite, respectively. This match of the $<110>_{FCC}$ // $<111>_{BCT}$ directions has already been determined in previous studies about the systems Fe-C and Fe-N [15,16]. Therefore, the Pitsch OR [16] is a suitable basis for the interpretation of the data presented in this work.

In martensite, a simple $[\bar{1}11]_{BCT}$ shear is generally considered to occur on the $(1\bar{1}2)_{BCT}$ plane [16]. This brings the question of whether a corresponding, i.e., matching $[\bar{1}10]_{FCC}$ shear exists on the $(110)_{FCC}$ plane in the FCC lattice. Such an FCC-to-FCT (cubic-to-tetragonal) transformation has indeed been reported for several alloy systems with martensitic transformations [57,58], e.g., in In-Tl [57] and Fe-Pd [58]. The underlying kinematics can be explained in terms of a double $<\bar{1}10>\{110\}$ shear mechanism which

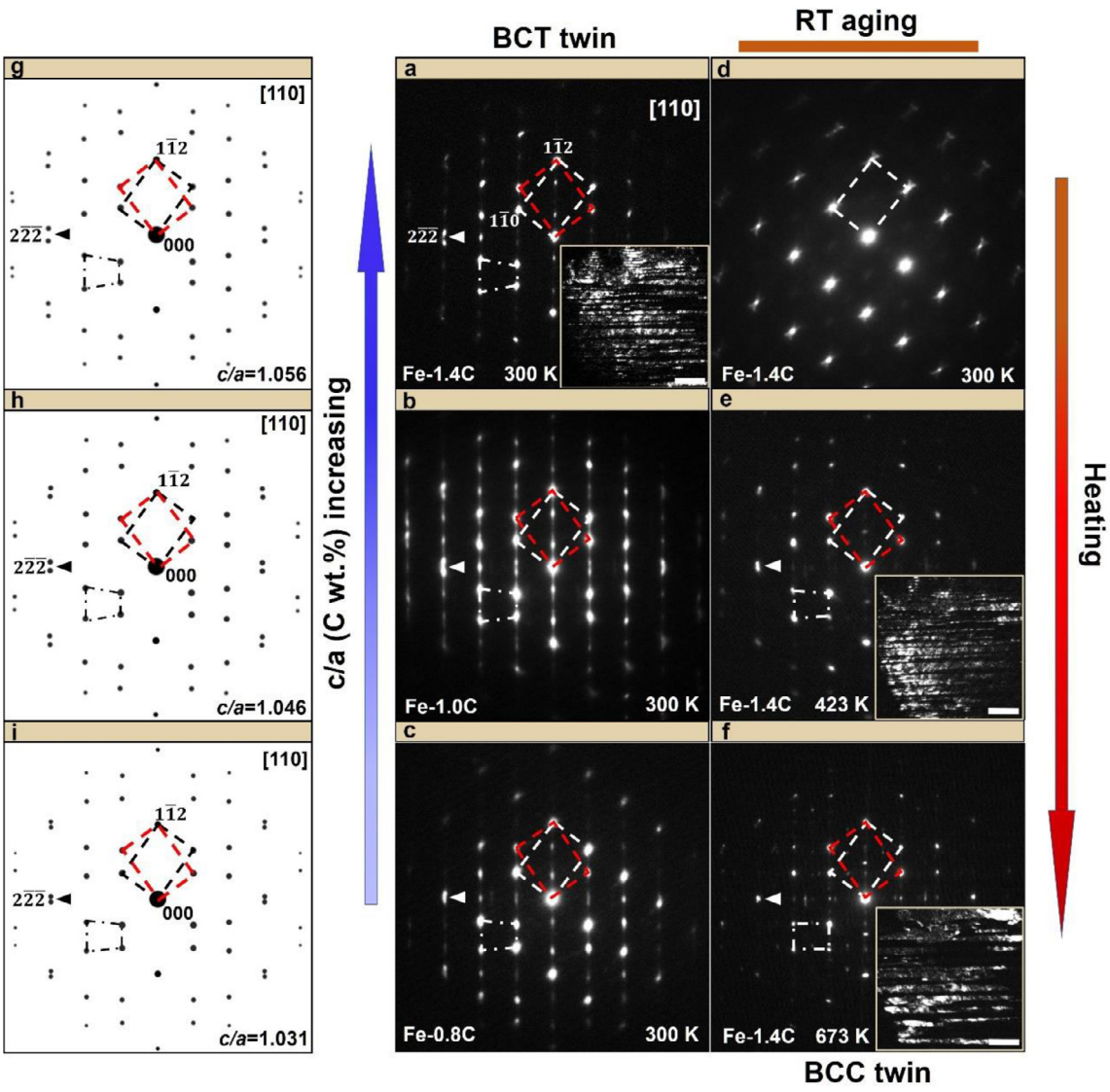

Fig. 4. SAED patterns of twinned martensite for materials with different C contents and heat treatment observed *in-situ* inside the TEM. (a–c) SAED patterns of BCT twin in the 1.4 C, 1.0 C, and 0.8 (wt.%) C specimens at 300 K. (a, e, and f) *in-situ* heating TEM observation of the 1.4 C specimen from 300 K to 673 K at a heating rate of approximately 15 K/min. Images of (e and f) were observed after keeping the temperature at 423 K and 673 K for 20 min. Insets in (a, e, and f), which show the morphology of twinned martensite, are the corresponding dark-field images from the (1$\bar{1}$0) diffraction spot. The scale bar in the insets represents 100 nm. (d) SAED pattern of BCT martensite aged at room temperature for three days. (g, h, and i) calculated diffraction patterns of BCT twins with *c*/*a* ratios of 1.056, 1.046, and 1.031 without considering the double diffraction of twins.

triggers a cubic-tetragonal transition (FCC to FCT) [57]. With decreasing Pd content in Fe-Pd alloys, the phase transformation was reported to change from FCC-FCT to FCC-BCT and finally to FCC-BCC after quenching [58]. As in the Bain model, the FCC lattice can be understood as a special BCT lattice, with a *c*/*a* ratio equal to $\sqrt{2}$. Therefore, the FCT lattice ($c/a < 1$) [58] could also be regarded as a BCT lattice with a *c*/*a* ratio below $\sqrt{2}$. The FCC-to-BCT-to-BCC process can then be regarded as a sequence of stepwise transformation processes in the BCT lattice during which the *c*/*a* ratio approaches 1, hence finally matching that of the BCC lattice. Following the Pitsch OR and the consecutive $<\bar{1}10>\{110\}_{FCC}$ shears, we devised a model of the atomic motions as plausible shuffling pathways during the MT (See the shuffling model in Section 3.4.1 that follows), Fig. 5. The FCC to BCT or BCT twin transformation includes a $[\bar{1}10](110)_{FCC}$ shear, which involves a slip of partial dislocations 1/12 $[\bar{1}10]_{FCC}$ on the $(110)_{FCC}$ planes (a non-ideal BCT lattice (BCT') formed from FCC), and a pure distortion which is determined by the final structure. The term 'pure distortion' is used here, in accord with Refs. [16,22], to describe an overall shape change between the BCT' and the ideal BCT lattice of about 3.9% volume change. A set of Molecular Dynamics (MD) simulations with the atomic nature of the phase transition processes have been performed (Fig. 6) (see the Supplementary Materials for details), which strongly supports the atomic shuffling model suggested in Fig. 5.

If a full dislocation 1/2 $[\bar{1}10]_{FCC}$ slips continuously on the $(110)_{FCC}$ plane (Fig. 5(a)), then the atomic arrangements in the FCC lattice (a = 3.61 Å) will not be changed. When a partial dislocation 1/2n $[\bar{1}10]_{FCC}$ ($n > 1$) continuously slips on the $(110)_{FCC}$ plane, the atomic arrangements in the FCC lattice get distorted and the relative spacing among the atoms changes. The distorted FCC lattice elongates along either the $[100]_{FCC}$ or the $[010]_{FCC}$ directions and shrinks in the other direction after the (110) shear, known as the first shear in the double $<\bar{1}10>\{110\}_{FCC}$ shear mechanism [57]. Considering the FCC lattice as a special case of a BCT lattice, the $[\bar{1}10](110)$ shear mechanism is a process during which the

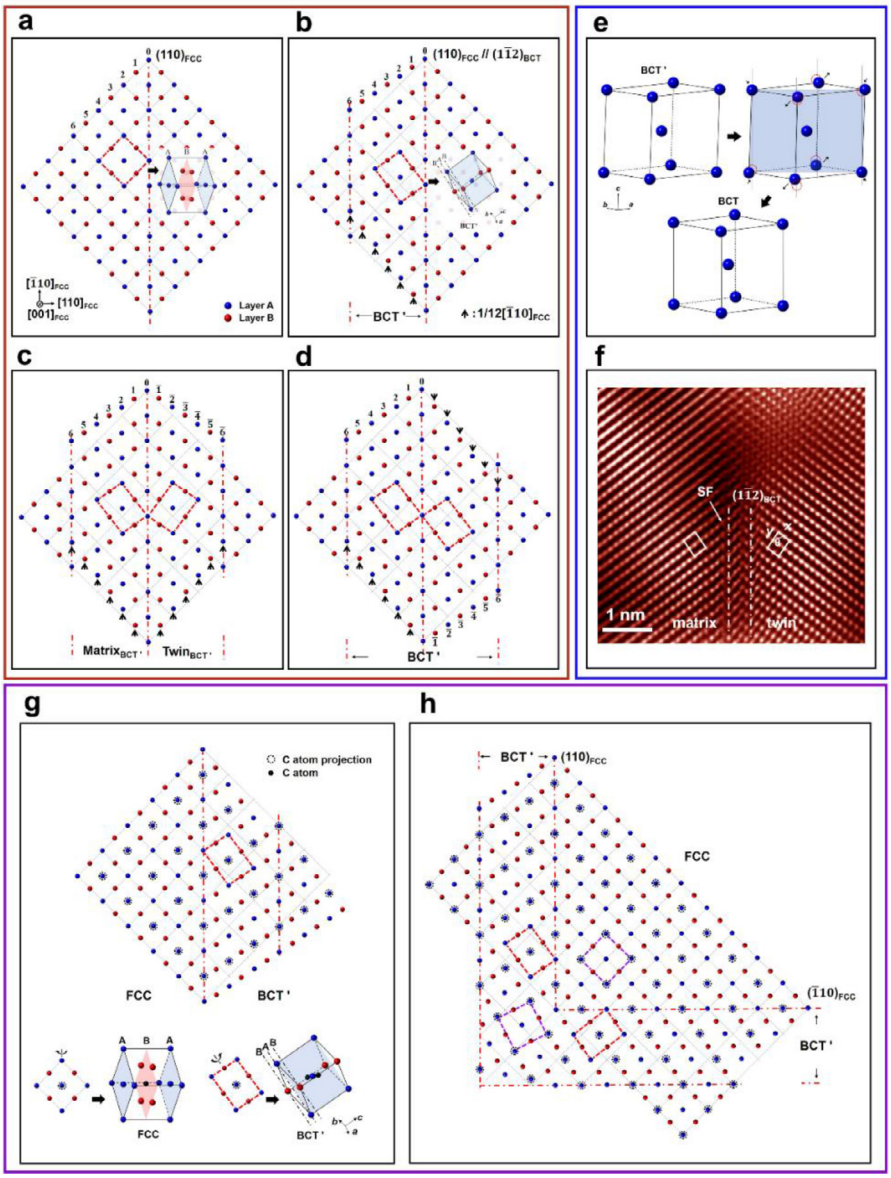

Fig. 5. Sketches of the atomic shuffling pathways for the individual atoms, as gathered from the experiments and considerations related to the underlying shear and distortion, to better explain the atomic position shifts from FCC to BCT and BCT twin ($c/a = 1.056$). (a) Atomic arrangement projection of the FCC lattice ($a = 3.61$ Å) along the $[001]_{FCC}$ direction; the illustration on the right is the stereogram of one FCC crystal cell. Blue and red dots indicate the atoms in two subsequent atomic layers (A and B layers), and the red dotted-dashed line indicates the 0th $(110)_{FCC}$ plane. (b) Atomic arrangement projection of FCC to BCT' with a $[\bar{1}10](110)_{FCC}$ shear; the illustration shows the stereogram of the BCT' structure. (c) Projection of FCC to BCT' twin. (d) Projection of BCT' growth. (e) Pure distortion of BCT' to BCT. (f) Inverse FFT image of an HRTEM image of the BCT twin lattice. (g) Atomic arrangement projection of the BCT' lattice as it is formed by the $[\bar{1}10](110)$ shear from the hosting FCC lattice under consideration of the occupation distribution of the C atoms. The stereogram of BCT' shows that the C atoms are located at the *c*-octahedral site of the BCT' lattice. (h) Symmetric double shears on the $(110)_{FCC}$ and $(\bar{1}10)_{FCC}$ planes in the FCC lattice.

c/a ratio in the BCT lattice is reduced when the size of the vector $1/2n\ [\bar{1}10]_{FCC}$ is very small. Also, the FCC lattice can transform into the BCT' by a continuous slip of partial dislocations $1/12\ [\bar{1}10]_{FCC}$ on $(110)_{FCC}$ planes as shown in Fig. 5(b). According to the shearing process, the lattice parameters and angles of the BCT' lattice cell are calculated as $a = b \approx 2.79$ Å, $c \approx 3.068$ Å, $\alpha \approx 92.43°$, $\beta \approx 87.57°$, and $\gamma \approx 99.4°$. This lattice is already very similar to the ideal BCT lattice with a c/a ratio of 1.056 ($c \approx 3.01$ Å, $a \approx 2.85$ Å). Furthermore, the BCT' lattice can be twinned or grown by the (110) shear in the positive or negative $[\bar{1}10]$ direction, as shown in Fig. 5(c, d). The total atomic displacements in the MT include an inhomogeneous shear [16,22] and a pure distortion [16,21,22] as has been suggested in several preceding works. The $[\bar{1}10](110)_{FCC}$ shear is considered the inhomogeneous part of the MT [16,22]. Therefore, to form the ideal BCT structure from BCT', pure distortion should occur. Fig. 5(e) shows a schematic diagram of the BCT' transformation into an ideal BCT structure ($c/a = 1.056$). By comparing their lattice parameters, the BCT' lattice could transform into the ideal BCT lattice after (i) an expansion in the $[001]_{FCC}$ and $[00\bar{1}]_{FCC}$ directions of approximately 11.6% of the atomic distances, (ii) a contraction in the $(110)_{FCC}$ plane distance of approximately 5.4%, and (iii) a decrease in the $[1\bar{1}0]_{FCC}$ direction of approximately 1.5%. After this pure distortion, the c/a ratio decreases from 1.1 in BCT' to 1.056 in BCT. The c/a ratio of BCT could be variable with different pure distortions and further decrease with the reduction of the $(110)_{FCC}$ plane distance. Fig. 5(f) shows a non-ideal BCT (BCT''): $x = 3.05$ Å, $y = 4.06$ Å, $\theta = 87°$) twin lattice image (Fe-1.4C) for comparison with the above transformation model.

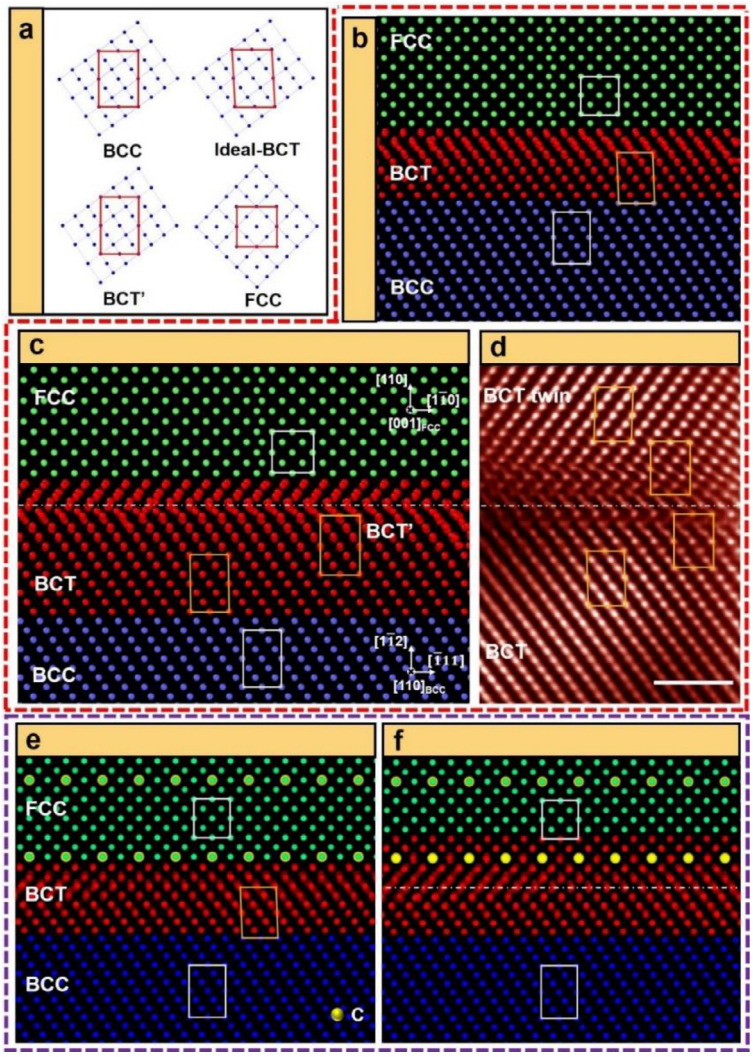

Fig. 6. MD simulation of the phase transition process for comparison with experiments. (a) Atomic arrangement projection of the BCC, ideal BCT, BCT', and FCC lattices along $[110]_{BCC/BCT}$ and $[001]_{FCC}$. (b) MD simulation image of crystal lattices after the first relaxation step viewed along $[001]_{FCC}//[110]_{BCC}$ using EAM potential. (c) MD simulation image after the second relaxation step. (d) HRTEM image of the BCT twin lattice for comparison with (c). The white scale bar in (d) represents 1 nm. (e and f) MD simulation images after two relaxation steps considering C atoms ($Fe_{16}C$, 5.9 at.% (1.33 wt.%)) in octahedral interstitial sites using the MEAM potential. (Large yellow circles in (e and f) denote C atoms)

The white line frame in Fig. 5(f) indicates a projection of the BCT" lattice cell similar to the red dashed line frame in Fig. 5(b). One stacking fault (SF) along the $[\bar{1}11]$ direction on the $(1\bar{1}2)$ plane is marked by an arrow. By comparison with Fig. 5(e), the BCT" lattice in Fig. 5(f) indicates that the lattice is in the pure distortion transition process. The atomic-scale TEM image provides direct support for the transformation model.

In order to describe the transformation process more accurately, lattice distortion matrixes are given as follows:

In the reference basis B_{FCC} (spanned by the vectors $[100]_{FCC}$, $[010]_{FCC}$, and $[001]_{FCC}$),

(a) The $[\bar{1}10](110)_{FCC}$ shear process from FCC to BCT' can be described as:

$$\begin{bmatrix}1&0&0\\0&1&0\\0&0&1\end{bmatrix}_{FCC}+\begin{bmatrix}1/6&1/6&0\\-1/6&-1/6&0\\0&0&0\end{bmatrix}_{FCC}\rightarrow\begin{bmatrix}7/6&1/6&0\\-1/6&5/6&0\\0&0&1\end{bmatrix}_{FCC} \quad (1)$$

$\begin{bmatrix}1/6&1/6&0\\-1/6&-1/6&0\\0&0&0\end{bmatrix}_{FCC}$ which refers to a $1/6\,[1\bar{1}0]_{FCC}$ shear on basic axes $[100]_{FCC}$ and $[010]_{FCC}$.

(b) The 'pure distortion' process includes three steps: (i) a contraction in the $(110)_{FCC}$ plane distance of approximately 5.4%, (ii) a decrease in the $[1\bar{1}0]_{FCC}$ direction of approximately 1.5%, (iii) an expansion in the $[001]_{FCC}$ and $[00\bar{1}]_{FCC}$ directions of approximately 11.6% of the atomic distances ($c/a = 1.056$).

The contraction of (i) is: $\begin{bmatrix}-1/36&-1/36&0\\-1/36&-1/36&0\\0&0&0\end{bmatrix}_{FCC}$, which equals a $1/36\,[\bar{1}\bar{1}0]_{FCC}$ shear on basic axes $[100]_{FCC}$ and $[010]_{FCC}$.

Then, the BCT' lattice changes to BCT'_1:

$$\begin{bmatrix}7/6&1/6&0\\-1/6&5/6&0\\0&0&1\end{bmatrix}_{FCC}+\begin{bmatrix}-1/36&-1/36&0\\-1/36&-1/36&0\\0&0&0\end{bmatrix}_{FCC}\rightarrow\begin{bmatrix}41/36&5/36&0\\-7/36&29/36&0\\0&0&1\end{bmatrix}_{FCC} \quad (2)$$

The decrease of (ii) is: $\begin{bmatrix} -1/30 & -1/50 & 0 \\ 1/30 & 1/50 & 0 \\ 0 & 0 & 1 \end{bmatrix}_{FCC}$, which means that the lattice decreases the atomic distance of $[\bar{1}10]_{FCC}$ to fit that of $[1\bar{1}\bar{1}]_{BCT}$.

Then, the BCT_1' lattice changes to BCT_2':

$$\begin{bmatrix} 41/36 & 5/36 & 0 \\ -7/36 & 29/36 & 0 \\ 0 & 0 & 1 \end{bmatrix}_{FCC} + \begin{bmatrix} -1/30 & -1/50 & 0 \\ 1/30 & 1/50 & 0 \\ 0 & 0 & 1 \end{bmatrix}_{FCC} \rightarrow \begin{bmatrix} 199/180 & 107/900 & 0 \\ -29/180 & 743/900 & 0 \\ 0 & 0 & 1 \end{bmatrix}_{FCC} \quad (3)$$

The expansion matrix of (iii) is: $\begin{bmatrix} 1 & 0 & 0 \\ 0 & 1 & 0 \\ 0 & 0 & 48/43 \end{bmatrix}$.

Then, the BCT_2' lattice changes to BCT:

$$\begin{bmatrix} 199/180 & 107/900 & 0 \\ -29/180 & 743/900 & 0 \\ 0 & 0 & 1 \end{bmatrix}_{FCC} \begin{bmatrix} 1 & 0 & 0 \\ 0 & 1 & 0 \\ 0 & 0 & 48/43 \end{bmatrix} \rightarrow \begin{bmatrix} 199/180 & 107/900 & 0 \\ -29/180 & 743/900 & 0 \\ 0 & 0 & 48/43 \end{bmatrix}_{FCC} \quad (4)$$

The 'pure distortion' process is determined by the final structure with different C contents. Therefore, the distortion matrix of this process is not a fixed value. However, different 'pure distortion' processes can perform similar operations.

In summary, the matrix transformation from FCC to BCT ($c/a = 1.056$) is:

$$\begin{bmatrix} 1 & 0 & 0 \\ 0 & 1 & 0 \\ 0 & 0 & 1 \end{bmatrix}_{FCC} \xrightarrow{1} \begin{bmatrix} 7/6 & 1/6 & 0 \\ -1/6 & 5/6 & 0 \\ 0 & 0 & 1 \end{bmatrix}_{FCC} \xrightarrow{2} \begin{bmatrix} 199/180 & 107/900 & 0 \\ -29/180 & 743/900 & 0 \\ 0 & 0 & 48/43 \end{bmatrix}_{FCC}$$

1: The first shear process from FCC to BCT'. 2: The second 'pure distortion' process from BCT' to BCT.

3.5. BCT martensite and ordering of C atoms

The BCT structure and its degree of tetragonality are significantly dependent on the specific ordering of the C atoms on the octahedral sites of the BCC lattice [35,39,52,54]. C atoms preferentially occupy the octahedral interstitial sites at 1/2 $<100>_{BCC}$ along one of the three sublattices in the BCC lattice [35,39,52,54]. If the C atoms are randomly distributed across the three types of octahedral sites, the lattice assumes a state of hydrostatic expansion, realized by the symmetric elongation along all the three basic axes, so that the structure maintains its BCC lattice [52]. Conversely, the lattice assumes increasing tetragonality when one of the basic axes has a higher degree of occupation by C atoms (turning it into a BCT lattice). The c/a ratio of such a BCT lattice reaches a maximum in tetragonality when the C atoms completely occupy only one type of octahedral sites [35,52,54]. In austenite (FCC lattice), the C atoms assume a regular solid solution with a disordered distribution of the C across all octahedral sites. The MT realized by quenching then leads to the transformation of these C atoms into an ordered distribution in their new structure [35,39,54]. Fig. 5(g) shows the sketched atomic arrangement projection along the $[001]_{FCC}$ direction of FCC to BCT' under consideration of the positions of the C atoms. An assumption here is that one FCC crystal cell contains one C atom located at an octahedral site (Fe_4C). When the FCC structure transforms into BCT' after the $[\bar{1}10](110)$ shear, the originally disordered distribution of C atoms in the FCC lattice becomes inevitably ordered in the BCT' lattice (Fig. 5(g)). In contrast, a pure distortion of BCT' to BCT does not change the positions of C atoms in this specific arrangement. Therefore, the inhomogeneous shear is the controlling process that explains the ordering of the C atoms, as revealed by the atomic motions during the MT (Fig. 5(g)).

Of course, the C content for the case of the here assumed Fe_4C composition (Fig. 5(g)) has been exaggerated, even for the case of high-carbon steels [59]. When the C content is between 0.9 wt.% (4.02 at.%) to 1.8 wt.% (7.79 at.%), approximately six to three FCC cells contain one C atom ($Fe_{24}C$ to $Fe_{12}C$). C atoms can affect the 2–3 interlayer spacings of the slip planes in FCC [60]. Therefore, 4–6 slip planes around the C atoms could be affected. This is generally consistent with our atomic shuffling model (Fig. 5) which assumes a 6-layer sequence of (110) planes as the reconstruction period. This is roughly equal to one C atom affecting three to six FCC cells, and it is consistent with the C content in high-carbon steels. The decrease of the c/a ratio is considered to be related to the order-disorder transition of C atoms [35,54]. As in a previous study, the disordering of C atoms can occur in two ways [35,39,52,54]: lattice conjugation and coherence between different variants of martensite [35,54] and short-range diffusion of C atoms [35,39,52]. Fig. 5(h) shows a double shear scenario on the $(110)_{FCC}$ and $(\bar{1}10)_{FCC}$ planes, and two BCT' variants are generated accordingly. The ordered arrangements of the C atoms in two BCT' variants are perpendicular to each other along the $[001]_{FCC}$ projection. Considering the three basic axes $<001>_{FCC}$, a total of 12 BCT' variants could form after multiple $<\bar{1}10>\{110\}$ shears. Multiple shears could introduce disorder in the occupation positions of C atoms along the three mutually perpendicular axes. Vice versa, activation of only a single prevalent $<\bar{1}10>\{110\}$ shear system can introduce maximum ordering of C atoms, and the ordering of C atoms decreases with the occurrence of multiple shears in the FCC lattice. In the case of a symmetric double shear scenario (Fig. 5(h)), the atomic arrangements of the so deformed lattice in the region where the two shears add up remain in a perfect FCC structure, similar to that of the region unaffected by shear (purple line frames in Fig. 5(h)). Two twinned martensite variants perpendicular to each other induced by double shears (Fig. 5(h)) are also observed in the TEM experiment (Fig. S4) and provide important support for this kinematic picture. The short-range diffusion of C atoms is considered as another important order-disorder process [35,39,52]. During ageing at RT, C atoms remain on their octahedral sites but undergo spinodal decomposition prior to carbide precipitation, reducing the tetragonality of the BCT lattice only modestly during the first decomposition stages [53,55]. With increasing temperature, some diffusing C atoms begin to form nanoscale carbides, which decreases the lattice's tetragonality and extra diffraction spots appear in the SAED pattern (Fig. 4(e)).

4. Conclusion

We propose a new phase transformation mechanism based on TEM observation and a corresponding transformation analysis of $(1\bar{1}2)$ BCT twinned martensite in carbon steels. An atomic shuffling model is developed to explain the atomic motion process during the MT by considering both, the symmetry features of the BCT twins and OR studies between martensite and austenite. The process step transforming the lattice from FCC to BCT or rather to BCT twins includes an inhomogeneous $<\bar{1}10>\{110\}_{FCC}$ shear and a pure distortion, which follows the Pitsch OR. The degree of C atomic ordering in the BCT structure can reach a maximum after a single $<\bar{1}10>\{110\}$ shear in FCC, and this ordering decreases with the occurrence of multiple shears. Elucidating the underlying phase transformation mechanism and atomic motions behind this

probably most important metallurgical transformation can guide the structural control and material design of a wide class of metals and alloys.

Author contributions

T.W. Liu performed the experiments, L.W. Liang and T.W. Liu conducted the MD simulation. T.W. Liu, D. Raabe, and L.H. Dai discussed the results, analyzed the data, and wrote the paper and the supplementary information.

Declaration of Competing Interest

The authors declare that they have no conflict of interest.

Acknowledgements

This work was financially supported by the NSFC (Nos. 51931005, 51901235, 11790292), the NSFC Basic Science Center Program for "Multi-scale Problems in Nonlinear Mechanics" (No. 11988102), the Key Research Program of Frontier Sciences (No. QYZDJSSW-JSC011), the Strategic Priority Research Program of the Chinese Academy of Sciences (No. XDB22040302), and the CityU grant 9360161.

T.W. Liu thanks Prof. X.L. Wu for the valuable discussion. Atom probe tomography research was conducted at the Inter-University 3D Atom Probe Tomography Unit of City University of Hong Kong.

Supplementary materials

Supplementary material associated with this article can be found, in the online version, at doi:10.1016/j.jmst.2022.06.023.

References

[1] J. Xia, Y. Noguchi, X. Xu, T. Odaira, Y. Kimura, M. Nagasako, T. Omori, R. Kainuma, Science 369 (2020) 855–858.
[2] S.H. Jiang, H. Wang, Y. Wu, X.J. Liu, H.H. Chen, M.J. Yao, B. Gault, D. Ponge, D. Raabe, A. Hirata, M.W. Chen, Y.D. Wang, Z.P. Lu, Nature 544 (2017) 460–464.
[3] A.L. Lai, Z. Du, C.L. Gan, C.A. Schuh, Science 341 (2013) 1505–1508.
[4] D. Raabe, C.C. Tasan, E.A. Olivetti, Nature 575 (2019) 64–74.
[5] H.Y. Chen, Y.D. Wang, Z.H. Nie, R.G. Li, D.Y. Cong, W.J. Liu, F. Ye, Y.Z. Liu, P.Y. Cao, F.Y. Tian, X. Shen, R.H. Yu, L. Vitos, M.H. Zhang, S.L. Li, X. Zhang, H. Zheng, J.F. Mitchell, Y. Ren, Nat. Mater. 19 (2020) 712–718.
[6] Y. Li, D.S. Martín, J.L. Wang, C.C. Wang, W. Xu, J. Mater. Sci. Technol. 91 (2021) 200–214.
[7] B. Hua, H.W. Luo, F. Yang, H. Dong, J. Mater. Sci. Technol. 33 (2017) 1457–1464.
[8] H.K.D.H. Bhadeshia, R. Honeycombe, in: Steels Microstructure and Properties, third ed., Butterworth-Heinemann, Oxford, 2006, pp. 95–128.
[9] G. Krauss, Steels: Processing, Structure, and Performance, ASM International, Almere, 2005.
[10] K. Otsuka, C.M. Wayman, Shape Memory Materials, Cambridge University Press, Cambridge, 1999.
[11] S. Djaziri, Y. Li, G.A. Nematollahi, B. Grabowski, S. Goto, C. Kirchlechner, A. Kostka, S. Doyle, J. Neugebauer, D. Raabe, G. Dehm, Adv. Mater. 28 (2016) 7753–7757.
[12] P. Kürnsteiner, M.B. Wilms, A. Weisheit, B. Gault, E.A. Jägle, D. Raabe, Nature 582 (2020) 515–519.
[13] T. Stech-Wheeler, J.D. Muhly, K.R. Maxwell-Hyslop, R. Maddin, Am. J. Archaeol. 85 (1981) 245–268.
[14] E.C. Bain, Trans. AIME 70 (1924) 25–46.
[15] G. Kurdjumov, G. Sachs, Zeit. F. Phys. 64 (1930) 325–343.
[16] W. Pitsch, Philos. Mag. 4 (1959) 577–584.
[17] A.J. Bogers, W.G. Burgers, Acta Metall. 12 (1964) 255–261.
[18] G.B. Olson, M. Cohen, Metall. Mater. Trans. A 7 (1976) 1905–1914.
[19] J.B. Yang, Z.G. Yang, Y. Nagai, M. Hasegawa, Acta Mater. 58 (2010) 1599–1606.
[20] C. Zener, Phys. Rev. 74 (1948) 639–647.
[21] J.S. Bowles, J.K. Mackenzie, Acta Metall. 2 (1954) 224–234.
[22] M.S. Wechsler, Acta Metall. 7 (1959) 793–802.
[23] M.A. Jaswon, J.A. Wheeler, Acta Cryst. 1 (1948) 216–224.
[24] C. Cayron, Acta Cryst. A 69 (2013) 498–509.
[25] Y.P. Gao, Y.Z. Wang, Phys. Rev. Mater. 2 (2018) 093611.
[26] A. Shibata, T. Furuhara, T. Maki, Acta Mater. 58 (2010) 3477–3492.
[27] B.R.J. Sandvik, C.M. Wayman, Metall. Trans. A 14A (1983) 835–844.
[28] G. Kurdjumov, E. Kaminsky, Nature 122 (1928) 476.
[29] O. Sherby, J. Wadsworth, D.R. Lesuer, C.K. Syn, Mater. Trans. 49 (2008) 2016–2027.
[30] P.M. Kelly, J. Nutting, Proc. Roy. Soc. A 259 (1960) 45–58.
[31] T.W. Liu, D.H. Ping, T. Ohmura, M. Ohnuma, J. Mater. Sci. 53 (2018) 2976–2984.
[32] A. Stormvinter, P. Hedström, A. Borgenstam, J. Mater. Sci. Technol. 29 (2013) 373–379.
[33] L.M. Hsiung, D.H. Lassila, Acta Mater. 48 (2000) 4851–4865.
[34] X. Wang, J.W. Wang, Y. He, C.M. Wang, L. Zhong, S.X. Mao, Nat. Commun. 11 (2020) 2497.
[35] G.V. Kurdjumov, A.G. Khachaturyani, Acta Metall. 23 (1975) 1077–1088.
[36] P. Maugis, D. Connétable, P. Eyméoud, Scr. Mater. 194 (2021) 113632.
[37] C.W. Sinclair, M. Perez, R.G.A. Veiga, A. Weck, Phys. Rev. B 81 (2010) 224204.
[38] P. Maugis, Acta Mater. 158 (2018) 454–465.
[39] A. Udyansky, J. von Pezold, V.N. Bugaev, M. Friák, J. Neugebauer, Phys. Rev. B 79 (2009) 224112.
[40] X.S. Yang, S. Sun, X.L. Wu, E. Ma, T.Y. Zhang, Sci. Rep. 4 (2014) 6141.
[41] X.S. Yang, S. Sun, T.Y. Zhang, Acta Mater. 95 (2015) 264–273.
[42] H. Fu, S.Q. Yuan, W. Sun, J.Q. Wan, K.C. Chan, J.M. Zhu, X.S. Yang, Scr. Mater. 204 (2021) 114153.
[43] T. Burkert, L. Nordström, O. Eriksson, O. Heinonen, Phys. Rev. Lett. 93 (2004) 027203.
[44] E.P. George, D. Raabe, R.O. Ritchie, Nat. Rev. Mater. 4 (2019) 515–534.
[45] E.K. Delczeg-Czirjak, A. Edström, M. Werwiński, J. Rusz, N.V. Skorodumova, L. Vitos, O. Eriksson, Phys. Rev. B 89 (2014) 144403.
[46] J.P. Yang, L.W. Jiang, Z.H. Liu, Z. Tang, A.H. Wu, J. Mater. Sci. Technol. 113 (2022) 61–70.
[47] C.D. Zhao, J.S. Li, Y.D. Liu, X. Ma, Y.J. Jin, W.Y. Wang, H.C. Kou, J. Wang, J. Mater. Sci. Technol. 86 (2021) 117–126.
[48] C. Liu, W.Y. Peng, C.S. Jiang, H.M. Guo, J. Tao, X.H. Deng, Z.X. Chen, J. Mater. Sci. Technol. 35 (2019) 1175–1183.
[49] J. Speer, D.K. Matlock, B.C. De Cooman, J.G. Schroth, Acta Mater. 51 (2003) 2611–2622.
[50] L. Morsdorf, C.C. Tasan, D. Ponge, D. Raabe, Acta Mater. 95 (2015) 366–377.
[51] M. Herbig, D. Raabe, Y.J. Li, P. Choi, S. Zaefferer, S. Goto, Phys. Rev. Lett. 112 (2014) 126103.
[52] X. Zhang, H.C. Wang, T. Hickel, J. Rogal, Y.J. Li, J. Neugebauer, Nat. Mater. 19 (2020) 849–854.
[53] K.A. Taylor, L. Chang, G.B. Olson, G.D.W. Smith, M. Cohen, J.B. Vander Sande, Metall. Trans. A 20 (1989) 2717–2737.
[54] G.V. Kurdjumov, A.G. Khachaturyan, Metall. Trans. 3 (1972) 1069–1075.
[55] S.B. Ren, T. Tadaki, K. Shimizu, X.T. Wang, Metall. Mater. Trans. 26 (1995) 2001–2005.
[56] W.Z. Zhang, Metall. Mater. Trans. 44 (2013) 4513-4131.
[57] J.S. Bowles, C.S. Barrett, L. Guttman, JOM 188 (1950) 1478–1485.
[58] M. Sugiyama, R. Oshima, F.E. Fujita, Trans. Jpn. Inst. Met. 25 (1984) 585–592.
[59] D. Raabe, B. Sun, A.K. Da Silva, B. Gault, H.W. Yen, K. Sedighiani, P.T. Sukumar, I.R.S. Filho, S. Katnagallu, E. Jägle, P. Kürnsteiner, N. Kusampudi, L. Stephenson, M. Herbig, C.H. Liebscher, H. Springer, S. Zaefferer, V. Shah, S.L. Wong, C. Baron, M. Diehl, F. Roters, D. Ponge, Metall. Mater. Trans. A 51 (2020) 5517–5586.
[60] R.W. Xie, W. Li, S. Lu, Y. Song, L. Vitos, J. Phys.-Condens. Matter 31 (2019) 065703.